eNeuro

Research Article: New Research | Disorders of the Nervous System

Background EEG connectivity captures the time-course of epileptogenesis in a mouse model of epilepsy

https://doi.org/10.1523/ENEURO.0059-19.2019

Cite as: eNeuro 2019; 10.1523/ENEURO.0059-19.2019

Received: 18 February 2019
Revised: 12 May 2019
Accepted: 30 May 2019

1. Title
Background EEG connectivity captures the time-course of epileptogenesis in a mouse model of epilepsy

2. Abbreviated Title
Epileptogenesis in a mouse model of epilepsy

3. List of authors
P. Słowiński,[1,2,3] L. Sheybani,[4] C.M. Michel,[4,5] M.P. Richardson,[6] C. Quairiaux,[4,7] J.R. Terry,[1,2,3,+] M. Goodfellow[1,2,3,+]

[1] College of Engineering, Mathematics and Physical Sciences, University of Exeter, Exeter, EX4 4QF, UK

[2] Centre for Biomedical Modelling and Analysis, University of Exeter, Exeter, EX4 4QD, UK

[3] EPSRC Centre for Predictive Modelling in Healthcare, University of Exeter, Exeter, EX4 4QD, UK

[4] Functional Brain Mapping Lab, Department of Fundamental Neuroscience, Campus Biotech, University of Geneva, 1202 Geneva, Switzerland

[5] Centre for Biomedical Imaging (CIBM), Lausanne and Geneva, 1015 Lausanne, Switzerland

[6] Institute of Psychiatry, Psychology and Neuroscience, King's College London, London, WC2R 2LS, UK

[7] Department of Fundamental Neuroscience, Faculty of Medicine, 1206 Geneva, Switzerland

[+] JRT and MG contributed equally to this work and are last authors on this work

4. Author contributions: JRT, MG., CMM and MPR. funding acquisition, PS, LS, CMM, MPR, CQ, JRT and MG designed the study, LS and CQ performed experiments, PS, MG and JRT conceived the model, PS analysed data, PS and MG writing – original draft, PS, LS, CMM, MPR, CQ, JRT and MG writing – review and editing. JRT and MG contributed equally to this work and are last authors on this work

5. Correspondence should be addressed to (include email address):
Piotr Słowiński p.m.slowinski@exeter.ac.uk

6. Number of Figures
Four figures in the main article, two figures in extended data

7. Number of Tables
Two tables

8. Number of Multimedia: None
9. Number of words for Abstract: 144
10. Number of words for Significance Statement: 69
11. Number of words for Introduction: 699
12. Number of words for Discussion: 951

13. Acknowledgments

14. Conflict of interests
The authors declare no competing financial interests.

15. Funding sources
PS, LS, CM, MPR, JRT and MG acknowledge the support of Epilepsy Research UK via grant P1505 ("An optimal model for focal onset epilepsies"). LS was supported by the Swiss National Science Foundation (grant 323530-158125). MPR is supported by the National Institute for Health Research (NIHR) Biomedical Research Centre at the South London and Maudsley NHS Foundation Trust. CMM is supported by the Swiss National Science Foundation (grant 320030-159705), by the National Centre of Competence in Research (NCCR) “SYNAPSY”, and by the Centre for Biomedical Imaging (CIBM) from Geneva and Lausanne. CQ is supported by the Foundation Ernst et Lucie Schmidheiny and by the Swiss League Against Epilepsy. MG, MPR and JRT gratefully acknowledge funding from the Medical Research Council via grant MR/K013998/1. MPR and JRT further acknowledge the financial support of the EPSRC via grant EP/N014391/1. The contribution of PS, MG and JRT was further generously supported by the Wellcome Trust Institutional Strategic Support Awards (204909/Z/16/Z and WT105618MA).

Abstract

Large-scale brain networks are increasingly recognized as important for the generation of seizures in epilepsy. However, how a network evolves from a healthy state through the process of epileptogenesis remains unclear. To address this question, here, we study longitudinal epicranial background EEG recordings (30 electrodes, EEG free from epileptiform activity) of a mouse model of mesial temporal lobe epilepsy. We analyse functional connectivity networks and observe that over the time-course of epileptogenesis the networks become increasingly asymmetric. Furthermore, computational modelling reveals that a set of nodes, located outside of the region of initial insult, emerges as particularly important for the network dynamics. These findings are consistent with experimental observations, thus demonstrating that ictogenic mechanisms can be revealed on the EEG, that computational models can be used to monitor unfolding epileptogenesis and that both the primary focus and epileptic network play a role in epileptogenesis.

Significance Statement

We provide the first description of how functional connectivity and network dynamics inferred from background EEG evolve during epileptogenesis. We focus on background EEG because it allows for direct comparison of functional networks before and after experimental intervention. We show that network dynamics inferred by means of computational modelling are different at early and later stages of epileptogenesis. Our findings provide further support for clinical potential of background EEG.

Introduction

Epilepsy is the most common chronic brain disorder affecting around 1 in 100 people worldwide and accounting for 0.6% of the global burden of disease (World Health Organization, 2019). Epilepsy is characterised by recurrent seizures. Seizure recurrence is a particularly important feature, because up to 10% of people worldwide, who do not have epilepsy, have a single seizure during their lifetime (World Health Organization, 2019). In other words, although every brain is able to generate seizures, not every brain is ictogenic, i.e., prone to generating recurring seizures.

Occurrences of epileptiform activity are irregular and unpredictable, but in contrast background brain activity (i.e. periods of activity that are free from obvious epileptiform abnormalities or discharges) is readily observable There is therefore a significant research effort focused on exploiting the background activity in research and clinical practice. Recent developments in this area, based on the modern, network perspective of epilepsy, have focused on functional network analyses of background EEG and MEG. These studies have revealed altered networks in the background EEG of people with epilepsy when compared to healthy controls (Chowdhury et al., 2014; Schmidt et al., 2014; Coito et al., 2015; Niso et al., 2015; Woldman and Terry, 2015; Schmidt et al., 2016; Soriano et al., 2017) and have uncovered specific features that can help point to the location of an "epileptogenic zone" within networks (van Dellen et al., 2014; Englot et al., 2015; Nissen et al., 2017). The studies above are predominantly concerned with uncovering differences between the EEG of people with epilepsy and healthy controls, and address the question of how ictogenic mechanisms manifest in the EEG. The latter are mechanisms that lead the brain of someone with epilepsy to sporadically transition into seizures from the non-seizure state.

However, a key questions in epilepsy research that remains is how does the brain becomes capable of generating recurrent seizures in the first place? This is a question of epileptogenic mechanisms, i.e. what changes does the brain undergo over longer periods of time in order to become ictogenic (Dichter, 2009; Lopes Da Silva et al., 2012; Goldberg and Coulter, 2013; Löscher et al., 2015). Various animal models can be used to explore these mechanisms. Gill et al. 2017, for example, studied a rat model of intraperitoneally administered kainic acid and catalogued the development of alterations to networks derived from fMRI (Gill et al., 2017). However, our understanding of the ways that large-scale brain dynamics evolve following local insult remains poor.

To address this, we study background functional EEG networks in a well-established mouse model of temporal lobe epilepsy (Bouilleret et al., 1999; Riban et al., 2002; Arabadzisz et al., 2005; Gröticke et al., 2008; Häussler et al., 2012; Lévesque and Avoli, 2013). In this model, unilateral injection of kainic acid in the dorsal hippocampus induces a status epilepticus followed by gradual neurodegeneration at the injected hippocampus (Riban et al., 2002; Arabadzisz et al., 2005). Concomitantly, spontaneous epileptiform events can be measured on the EEG at both hippocampi and, after 2-8 weeks, spontaneous and recurrent paroxysmal discharges that are reminiscent of focal and secondarily generalized seizures occur (Riban et al., 2002; Arabadzisz et al., 2005; Chauvière et al., 2012; Huneau et al., 2013; Salami et al., 2014; Sheybani et al., 2018).

In the current study, we characterise functional connectivity networks before and during epileptogenesis by analysing EEG recorded before kainic acid injection as well as at 7 and 28 days after the injection. Our analysis reveals that the progression of epileptogenesis is reflected in changes to background functional connectivity networks, with the focal injection leading to a disruption of network symmetry. We use a mathematical model to understand how these observed changes affect the ways that different nodes contribute to generation of epileptiform activity. Using only the background activity as input to the model, it reveals that nodes outside of the injected hippocampus become more important throughout epileptogenesis. This is in line with previous experiments that demonstrated the emergence of epileptiform activity self-sustained by brain structures outside of the epileptic focus (the injected hippocampus) (Sheybani et al., 2018). These findings present a step towards a network level understanding of epileptogenesis that could be developed to aid diagnosis and treatment of epilepsy.

Materials and Methods

Animals and recordings

We used longitudinal recordings from the experiments described in (Sheybani et al., 2018). We analysed longitudinal recordings from 12 animals (adult male C57BL/6j mice, Charles River) for which data was recorded before unilateral kainic acid injection into the left hippocampus (Day 0) as well as at 7 and 28 days after injection. Of the 12 longitudinal datasets 1 was excluded from all analysis due to poor quality of the data. Out of the 11 remaining datasets 4 were excluded from analysis at day 7 due to high number of artefacts and noise in the background EEG. Therefore, we used a total of 11 datasets with recordings at day 0 and day 28, with 7 of the 11 datasets also including recordings at day 7. Additionally, we analysed data recorded from 4 sham control animals (adult male C57BL/6j mice, Charles River) that were unilaterally saline injected into the left hippocampus and had epicranial EEG recorded 28 days after the injection.

The epicranial EEG was recorded at 4kHz sampling frequency using Digital Lynx SX (Neuralynx, USA). All recordings were re-referenced to the electrode average. We removed power line interference using a 50Hz (and 100Hz and 150Hz harmonics) notch filter and further band-pass filtered the data between 1 and 150 Hz using a zero-phase forward and reverse Butterworth filter of order 2.

From each EEG recording, which lasted around 30 minutes, multiple 1 second background data segments were selected from periods without epileptiform activity (median number of segments 55, min 17, max 83); for data collected on days 7 and 28 the segments were at least 1 second removed from the onset of a generalised spike (GS - interictal epileptic discharges, see (Sheybani et al., 2018)).

All experiments described in (Sheybani et al., 2018) were conducted in accordance with Swiss Laws on animal experimentation.

Network reconstruction

As in (Rummel et al., 2015; Goodfellow et al., 2016; Schmidt et al., 2016) we treated each EEG channel as recording from a single node of a network. To estimate weights of directed connections between the nodes we combined methods presented in (Rummel et al., 2015; Schmidt et al., 2016). Namely, to measure statistical interdependency between the EEG channels we employed the cross-correlation function:

$$r(x_i,x_j)(t)=\begin{cases}\sum_{t=1}^{T-t} x_i(t+t)x_j(t), & t\geq 0,\\ \sum_{t=1}^{T-|t|} x_i(t)x_j(t+|t|), & t<0,\end{cases} \qquad (2)$$

$$r_{coeff}(x_i,x_j)(t)=\frac{r(x_i,x_j)(t)}{\sqrt{r(x_i,x_i)(0)r(x_j,x_j)(0)}}.$$

In practice, we used the Matlab function: `xcorr` with option `coeff`, which normalizes the cross-correlation function in such a way that the auto-correlations at zero lag are equal to 1.

To estimate the strength of the relationship between channels we used three different approaches based on the extremum of the cross-correlogram $r_{coeff}(x_i, x_j)(\tau)$. In the first method, we follow (Schmidt et al., 2016), and we use the maximum absolute value of the cross-correlogram, $\max_\tau |r_{coeff}(x_i, x_j)(\tau)|$. In the second method, we followed suggestion from (Sinha et al., 2017) and use only the values of $max_\tau |r_{coeff}(x_i, x_j)(\tau)|$ for which $r_{coeff}(x_i, x_j)(\tau)>0$. We refer to the matrices derived with these two methods as C^{ABS} and C^{MAX}, respectively. Finally, to understand the difference between the C^{ABS} and C^{MAX} we also analysed networks estimated using the values of $max_\tau |r_{coeff}(x_i, x_j)(\tau)|$ where $r_{coeff}(x_i, x_j)(\tau)<0$. We refer to the matrices from the third method as C^{MIN}.

The cross-correlogram $r_{coeff}(x_i, x_j)(\tau)$ provides a natural way to infer directionality of the estimated connections. The direction of the connections is given by the sign of the lag between the two channels; with $\tau < 0$ meaning that a channel i is leading (transmitting to)

channel *j*. In the paper we adopted notation in which a connection from channel *i* to *j* is noted as element c_{ij} of the connectivity matrix. In this convention, extrema of the cross-correlation function at $\tau < 0$ make up the elements of the matrix that are above the diagonal $j > i$ and ones at $\tau > 0$ are below the diagonal $i > j$. The diagonal is equal to 0 (no self-loops).

We disregarded any lags longer than 250ms (1000 points) and lags shorter than 2ms (8 time samples). We removed the shortest lags to address the problem of volume conduction, i.e. spurious correlations between the time series due to common sources of activity. Such activity is typically detected at very small values of lag between the time series. We chose 8 samples because they correspond to a single sample at sampling frequency 512Hz, which is a typical sampling frequency used in clinical acquisition of intracranial EEG.

To increase the accuracy of estimation of the connections, we divided each 1-second data segment into 21 windows (500ms) with 25ms overlap, and we computed connectivity matrices for each window.

We further checked that values of the coefficients were not solely due to the presence of dominant intrinsic channel frequencies. For each 1 second data segment we generated 100 sets of univariate Iterative Amplitude Adjusted Fourier Transform (IAAFT) surrogates (Schreiber and Schmitz, 1996), each containing 30 channels, generated using 10 iterations. A Wilcoxon rank sum test (with Bonferroni correction for 870 comparison) was used to test, element-wise, whether coefficients in the 21 windows had a different median than the 2100 surrogate windows. For each 1 second data segment the computed values of cross-correlation coefficients were averaged and normalized in the same way as in (Rummel et al., 2015),

$$c_{ij} = \frac{\left\langle c_{ij,data} \right\rangle - \left\langle c_{ij,surr} \right\rangle}{1 - \left\langle c_{ij,surr} \right\rangle} s_{ij}. \quad (3)$$

Here, $\langle c_{ij,data} \rangle$ is the median value of the coefficients from the data, $\langle c_{ij,surr} \rangle$ is the median value of the coefficients from the surrogate data, $s_{ij} = 1$ if the family wise error rate, FWER < 0.05 and 0 otherwise. Finally, we averaged the network topologies over all data segments in a recording and normalised the coefficients with the sum of all of the elements of the connectivity matrix. By averaging over multiple segments we aimed to estimate functional connectivity that accounts for complex bi-directional interactions between the brain regions generating the recorded activity.

To ensure that the variability in the number of data segments did not affect the presented results, we excluded from analysis 5 data sets that either had a very low number of data segments or resulted in a low number of connections, see Figure 1.

[Figure 1 around here]

Model

To model the network dynamics we followed the procedure presented in (Lopes et al., 2017, 2018), i.e. we analysed to what extent removal of a single node (virtual resection

(Goodfellow et al., 2016; Khambhati et al., 2016)) affects activity of the network that on average spends half of the time in the active state. The simulations proceeded as follows:

1.) The dynamics of each node was modelled using the theta model (Ermentrout and Kopell, 1986), which has been shown to well approximate the predictions of neural mass models close to a saddle-node on invariant circle bifurcation (Lopes et al., 2017):

$$\frac{d\theta}{dt} = 1-\cos\theta + (1-\cos\theta)I(t), \qquad I(t) = I_0 + I_{noise}\mathcal{N}(0,1). \tag{4}$$

Here, I_0 is the intrinsic model parameter, I_{noise} = 6 is noise intensity and $\mathcal{N}(0,1)$ is a random number from a normal distribution with mean 0 and variance 1. We set I_0 = -1.2 to ensure that in the absence of noise a stable steady state existed in the system. To couple the nodes, we used the functional connectivity matrix C; with elements c_{ij}. Coupled equations have the following form (Lopes et al., 2017):

$$\frac{d\theta_i}{dt} = 1-\cos\theta_i + (1-\cos\theta_i)I_i(t), \qquad I_i(t) = I_0 + I_{noise}\mathcal{N}_i(0,1) + \omega\sum_{j=1}^{N} c_{ji}[1-\cos(\theta_j-\theta_j^*)]/N. \tag{5}$$

Here, ω is a global scaling factor of the weights c_{ji} of the incoming connections of the node i; N is the total number of nodes in the network. The θ_j^* is the steady state of node j. Parameters I_0 = -1.2 and I_{noise} = 6 are the same at each node. For each simulation, we used a time step of 0.01, and the duration of the simulation was 4.0e6 time steps. See (Lopes et al., 2017) for more details.

2.) We first estimated the value of ω>0 for which on average the whole network spends 50% of the time in the active state. ω_{50} was estimated in separate simulations (averaged over 10 runs with independent noise realisation). We used the same definition of the node's active state as in (Lopes et al., 2017). To quantify activity of the whole network we use the brain network ictogenicty (BNI) which is the average time each node spends in the active state (Goodfellow et al., 2016):

$$BNI = \frac{1}{N}\sum_{i=1}^{N}\frac{time\ node\ i\ spent\ in\ active\ state}{duration\ of\ simulations}. \tag{6}$$

3.) We then removed a single node and ran simulations with exactly the same parameters; we normalised the sum in Eq. (5) with N rather than N-1 to keep the connection weights exactly the same. We measured the change in the network dynamics by comparing the time spent by the network in the active state before and after removing the node. To this end, we used node ictogenicity NI defined in (Goodfellow et al., 2016):

$$NI_i = \frac{0.5 - BNI_{i,post}}{0.5}, \tag{7}$$

where $BNI_{i,post}$ is the BNI estimated after removing node *i* from the network. We repeated each simulation 10 times and took the mean value of the NI over the 10 runs with independent noise realisations.

Statistical methods

We used non-parametric, median based statistical methods (Kruskal-Wallis, Mann-Whitney-Wilcoxon or Kolmogorov-Smirnov tests) throughout. To control for multiple comparison during network reconstruction we used the Bonferroni FWER with a significance level of 0.05 (Benjamini and Hochberg, 1995). To control for multiple comparison in the network analysis we used the Benjamini-Hochberg false discovery ratio (FDR) (Benjamini and Hochberg, 1995). Due to small sample sizes we used a significance level of 0.1 for the network analysis. We additionally quantified effect sizes using area under the receiver-operating characteristic (AUROC), which is a non-parametric alternative of the common-language effect size (Hentschke and Stüttgen, 2011). We used this method because it has a simple interpretation:

- AUROC=0.5 means that the scores in the two groups are identical;
- AUROC=0 means that all scores in the tested group are smaller than the scores of the control group;
- AUROC=1 means that all scores in the tested group are larger than the scores of the control group.

All presented significant results have AUROC < 0.2 or > 0.8 meaning that the overlap between the scores in the two groups is less than 20%. In other words, in 80% of the cases a random score from one group exceeds a random score from the other group (Hentschke and Stüttgen, 2011). For the non-parametric 1-way ANOVA analysis (Kruskal-Wallis test) we computed post-hoc AUROC effect sizes of differences between the groups.

To visualize relationships between individual functional connectivity matrices we first quantified pairwise similarity between them by computing the Frobenius distance (Golub and Loan, 1996) for all pairs of matrices,

$$\left\| A - B \right\|_F = \sqrt{\sum_{i=1}^{g} \sum_{j=1}^{gn} (a_{ij} - b_{ij})^2}, \quad (1)$$

where a_{ij} and b_{ij} are the elements of matrices A and B. Next, we used classical multidimensional scaling to visualize relations captured by the similarity matrix (Borg and Groenen, 2005), using Matlab (Matlab) function `cmdscale`.

Statistical Table

[Table 2 around here]

Code Accessibility

Matlab scripts for the network analysis are available on request from the PS. The model is subject to copyright owned by the University of Exeter (international patent application WO/2017029505).

Results

Our goal is to characterise the evolution of large-scale functional brain networks during epileptogenesis. Many measures exist to quantify functional connectivity (Wang et al., 2014), each with different underlying assumptions. We begin with no *a priori* knowledge regarding the way in which the evolving ictogenic mechanisms of the brain may be reflected in functional connectivity. We therefore do not restrict our analysis to a particular frequency band. Considering broadband signals, a natural way to quantify functional connectivity is to study the correlation between signals. To avoid problems associated with volume conductions, we use the cross-correlation function and exclude correlations with maximum at zero lag (Christodoulakis et al., 2015). Focussing on lagged correlations also gives a natural way to build directionality into the networks. Additionally, the resulting correlations can be positive or negative and there are therefore different ways to quantify strength of interactions in the derived functional network. First, one can quantify the strength of the connection using the maximum of the absolute value of the cross-correlogram (Schmidt et al., 2014). We refer to the networks estimated with this method as C^{ABS}. Second, one can neglect negative values (see e.g. reasoning presented in (Sinha et al., 2017)) and use only the values of C^{ABS} at which the cross-correlogram >0. We refer to networks estimated with this method as C^{MAX}. To analyse the differences between C^{ABS} and C^{MAX} one can also examine the networks derived from the values of C^{ABS} at which the cross-correlogram <0. We refer to these networks as C^{MIN}. In other words, one can decompose the connectivity matrices C^{ABS} into component matrices C^{MAX} and C^{MIN}. See Materials and Methods for details of the reconstruction of the connectivity matrices. In the following sections, we examine functional connectivity through epileptogenesis using these three methods.

Epileptogenesis changes properties of background functional connectivity networks

[Figure 2 around here]

Figure 2 demonstrates the evolution of functional connectivity across the first 4 weeks of epileptogenesis for the three types of networks introduced above. The functional connectivity is described by connectivity matrices: each entry in a connectivity matrix represents a statistical relationship (in this case the extremum of cross-correlogram that occurred for non-zero lag) between EEG signals at two different electrodes. Therefore, the connectivity matrix captures the correlation pattern of a multichannel EEG signal.

We quantified the differences between the connectivity matrices of individual animals across three different time points (days 0, 7 and 28) by calculating the Frobenius distance between them (see Materials and Methods for detailed description) (Borg and Groenen, 2005). Using these distances to visualize the similarity between the matrices reveals that control (Day 0 and Sham) networks are different to post-injection networks (days 7 and 28), since they form a distinct cluster compared to matrices derived from recordings at days 7 and 28 for each of the three measures (Fig. 2A, E, I). The clustering of points corresponding to matrices derived from recordings before and after injection visible in Fig. 2 A, E and I demonstrates that the kainic acid injection has a large and consistent effect on the correlation patterns of the epicranial EEG. The clusters, however, do not inform us about which components of the connectivity matrices have changed.

To study the data on the population level, we compute median correlation matrices for each time point (median over entries c_{ij} of the connectivity matrices). Fig. 2 demonstrates that the median correlation matrices appear to progress from an initially symmetric

arrangement at day 0, to asymmetric networks post-injection (days 7 and 28). It also shows that the C^{ABS} matrices are a composition of the C^{MAX} and C^{MIN} matrices and that the C^{MAX} and C^{MIN} matrices differ from each other. A characteristic feature of the C^{MAX} networks is that the connections between contralateral regions appear to be amongst the strongest connections (the top right and bottom left quadrants of the connectivity matrices in Fig. 2F-H). To quantify the redistribution of connections post-injection, we asked whether connections from each electrode to their contralateral equivalent (dark anti-diagonals of the quadrants) were among the strongest (i.e. in 5% of the strongest connections). For control networks, 38% of contralateral connections were among the strongest, whereas this percentage fell to 22% at days 7 and 28. This means that post-injection, the EEG between hemispheres becomes less synchronized. We note that this trend was also observed if we considered raw as opposed to normalised connectivity matrices. Such a decrease in synchronization has previously been shown for the hippocampi (Arabadzisz et al., 2005), but not for other brain regions. In contrast, for the C^{MIN} networks the strongest connections are ipsilateral, meaning that they represent connections within a hemisphere (top left and bottom right quadrants of the connectivity matrices in Fig. 2J-L).

[Figure 3 around here]

To quantify the breakdown of synchronization, we calculated the degree imbalance (outdegree-indegree) of nodes in the functional connectivity networks of individual animals. Degree imbalance is an aggregated measure that quantifies the strength of connectivity for each node. Statistically, if $\text{outdegree}_{\text{weighted}} > \text{indegree}_{\text{weighted}}$ the EEG signal recorded on a node temporally leads some of the other nodes and the node can be interpreted as a "source" of activity if not, the node lags other nodes on average and it can be considered a "sink" ($\text{outdegree}_{\text{weighted}} < \text{indegree}_{\text{weighted}}$).

Interestingly, although network topologies are different for each of the three methods considered, the degree imbalance of the C^{ABS}, C^{MAX} and C^{MIN} networks are similar. Figure 3A-C, E-G and I-K show the distribution of median degree imbalance across nodes. At day 0, the configuration is symmetric, with sinks (blue nodes in Fig. 3A, E and J) predominantly in anterior and posterior regions. The maximum absolute values of the degree imbalance at day 0 are approximately two times lower than at days 7 and 28. At day 7 the degree imbalance increases, with sources located at the left posterior and the right anterior regions. This pattern persists through to day 28. Interestingly, many of the nodes that became sources are located above the left hippocampus i.e. the site of initial intrahippocampal injection (Sheybani et al., 2018).

Figure 3A-C, E-G and I-K show the network toplogy of the top 5% of the strongest connections of the median connectivity matrices presented in Fig. 2. These network corroborate our observations based on the connectivity matrices: C^{ABS} matrices are a composition of the C^{MAX} and C^{MIN} matrices; the strongest connections in the C^{MAX} matrices are contralateral and the strongest connections in C^{MIN} matrices are ipsilateral. Taken collectively, Fig. 2 and Fig. 3 describe changes in symmetry of the connectivity matrix and illustrate the large-scale breakdown of synchronization between right and left hemispheres that can be revealed from background EEG through epileptogenesis.

In addition to analysing the degree imbalance of nodes, we analysed global properties of the functional connectivity networks; see Table 2 and Fig. 3D, H and L. For all three

types of network the same measures (Spectral norm, Variance of neighbour weighted outdegree and Degree of asymmetry) were found to be significantly different on day 0 and days 7 and 28 (FDR<0.05, Kruskal-Wallis test with Benjamini-Hochberg FDR correction for 19 tested network measures - chosen to capture in a non-redundant way the most important topological and spectral properties of the networks); see Table 2 for all the analysed measures. Values of these three measures increase over the time-course of epileptogenesis; as an example, Fig. 3D, H and L illustrate increasing median of the degree of asymmetry (Li and Zhang, 2012). These changes in local and global network properties further indicate that the underlying functional connectivity pattern of background activity becomes progressively more irregular and spatially heterogeneous post injection.

[Table 2 around here]

Epileptogenesis changes network dynamics

[Figure 4 around here]

An important question is how these alterations to the pattern of functional connectivity inferred from background EEG influence the ways that nodes contribute to the generation of epileptiform dynamics. To make this mechanistic link, we studied a mathematical model of spiking dynamics placed upon the nodes of networks derived from each animal (see Material and Methods). To measure the contribution that each node in a network has to the generation of epileptiform rhythms we use "Node Ictogenicity" (NI) introduced in (Goodfellow et al., 2016) (see Material and Methods). Figure 4 shows the distribution of NI at days 0, 7 and 28 for the three types of networks. At day zero, which we use as a reference point, we see that the NI is distributed symmetrically through the network, but with slightly elevated values in frontal regions. This means that, if the network was ictogenic, nodes in frontal regions would contribute more to the generation of epileptiform dynamics. At day 7, the C^{ABS} networks, shown in Fig. 4B, displays significantly higher NI for multiple nodes in the left posterior and right anterior regions. This pattern persists at day 28 (see Fig. 4C), though nodes with elevated NI are now constrained to fewer regions. For the C^{MAX} networks, illustrated in Fig. 4E and F significant increases in NI above baseline only occur at day 28. Finally, for the C^{MIN} networks, NI increases significantly at a single node, the location of which changes between days 7 and 28. On both days the node with significantly elevated NI resides within the region shown to be affected by the TTX silencing, as identified from Fig. 12B in (Sheybani et al., 2018). In the experiments described in (Sheybani et al., 2018) the kainate injected hippocampus (left) was silenced using an intrahippocampal TTX injection. After the TTX injection on day 7, interictal generalised spikes (GS) subsided. The same procedure on day 28 did not affect the frequency of occurrence of GS.

Generalised spikes are interictal epileptic discharges recently reported to be a predominant EEG marker of evolving abnormal dynamics during the latent as well as chronic phase of the disease in the Kainic acid model (Sheybani et al., 2018). GS travel across the whole epileptic network and have also been observed in humans (Aarts et al., 1984; Mohamed et al., 2001; Moseley et al., 2012). In (Sheybani et al., 2018) it was shown that the frequency of occurrence of GS increases during epileptogenesis and that their occurrence is correlated with increased jerky movements. Furthermore, by day 28 GS no longer depend on the activity of the injected hippocampus, which was captured in

the TTX silencing experiment and evolution of the location of their onsets throughout days 0 to 28, see Fig. 6E in (Sheybani et al., 2018). At day 7, GS originate predominantly from the left and right posterior regions, which are covered by the increase in NI in left posterior regions and also node 9 in the C^{ABS} networks. However, changes in NI are also observed in anterior regions in our model results. At day 28, GS originate predominantly from the right posterior regions, which is best captured by the evolution of NI in C^{MAX} networks.

Discussion

Network analyses are increasingly being used in order to refine diagnosis, prognosis and treatment for epilepsy (Schmidt et al., 2014; Englot et al., 2015; Niso et al., 2015; Rummel et al., 2015; Tracy and Doucet, 2015; Goodfellow et al., 2016; Schmidt et al., 2016; Smith and Schevon, 2016; Lopes et al., 2017, 2018). In humans, functional connectivity derived from the background EEG are known to be altered in epilepsy. For example (Englot et al., 2015) showed that patients with focal epilepsies (temporal and neocortical) had decreased resting-state functional connectivity in multiple brain regions. In addition, people with idiopathic generalized epilepsies, as well as their first-degree relatives, have been shown to have elevated mean-degree and mean-degree variance of background functional EEG networks (Chowdhury et al., 2014).

Here we have provided the first characterisation of how functional connectivity inferred from background EEG evolves during epileptogenesis. During epileptogenesis, functional connectivity networks that are initially regular and symmetric become irregular and asymmetric. This corresponds to a loss of functional connectivity between hemispheres, both in the normalised connectivity presented in Fig. 2 and if the raw connectivity is considered. These changes observed using EEG are in line with previous studies of fMRI functional connectivity derived in the tetanus toxin model (Otte et al., 2012), and could be underpinned by changes in white matter tracts (Otte et al., 2012) or changes to dynamics within localized brain regions. However, it differs from the analysis of the fMRI-derived functional connectivity in the systemic kainic acid model of TLE which displayed stronger connections in comparison with control animals (Gill et al., 2017). Potential reasons for these discrepancies include the intraperitoneal administration of kainic acid used in (Gill et al., 2017) causing more widespread changes in the brain tissue than intrahippocampal administration. Furthermore, functional networks reported in (Gill et al., 2017) were estimated using long duration recordings (tens of minutes vs seconds in our study) from anesthetized animals (awake head fixed animals in the current study). Additionally, neither of these previous studies addressed the process of epileptogenesis through repeated observations within the same animal.

To relate our findings of altered functional connectivity to the generation of epileptiform activity, we used a mathematical model. The model allowed us to define the relative contribution of nodes to the generation of epileptiform dynamics. Our model showed that the set of nodes that are important for epileptiform dynamics evolves over 4 weeks of epileptogenesis. Two of the three different methods we used to compute functional connectivity network revealed nodes outside of the injected hippocampus that were important contributors to epileptiform dynamics. Specifically, significant changes in the NI distribution of the C^{MIN} connectivity networks (at which the cross-correlogram <0) capture the increase of NI over the injected hippocampus, which occurs 7 days after the injection and persist through to day 28. In contrast, the C^{MAX} connectivity networks (at

which the cross-correlogram *>0)* reveal changes in the distribution of NI only at day 28, involving multiple nodes that are located outside the injected hippocampus.

We hypothesise that, C^{MIN} and C^{MAX} networks reflect two mechanisms that generate GS. The first mechanism is local and related to the initial insult (the injected hippocampus), whereas the other mechanism is distributed and is a consequence of network remodeling. Importantly, Fig. 4D-F show that the second mechanism emerges at a time subsequent to the initial insult. This interpretation is consistent with the results of (Sheybani et al., 2018) in which pharmacological silencing of the injected hippocampus at day 7 stopped GS, whereas it had no effect when performed at day 28. This suggests the evolving importance of a distributed network throughout epileptogeniesis. In other words, results of the modelling suggest that the injected hippocampus is driving the epileptiform activity at day 7, whereas at day 28 the activity is driven by both the injected hippocampus as well as the wider network.

Additionally, we note that changes in NI across individual nodes are directly interpretable in terms of generation of the GS and the results of the silencing experiments, while typical graph theory measures (e.g. degree imbalance or degree asymmetry) do not allow such direct interpretation. This observation provides further support for the use of mathematical models to uncover regions of the brain that are important for generating abnormal dynamics and to aid the interpretation of experimental and clinical data (Goodfellow et al., 2016; Schmidt et al., 2016; Bartolomei et al., 2017; Hebbink et al., 2017; Lopes et al., 2017; Melozzi et al., 2017; Proix et al., 2017; Lopes et al., 2018). A natural next step would be to model the process of epileptogenesis itself to better understand why these changes occur, and why they occur in specific brain regions. Insights into spatial and temporal evolution of epileptogenesis could help to develop new treatments (Dichter, 2009; Lowenstein, 2009; Löscher and Brandt, 2010; Lopes Da Silva et al., 2012; Goldberg and Coulter, 2013; Löscher et al., 2015) and uncover reasons for seizure recurrence after epilepsy surgery (Mathon et al., 2017).

We express caution in relating observations made in this study to human epilepsy, as we expect mouse epicranial EEG contains contributions from brain structures that are subcortical in humans (e.g. hippocampus) and therefore would contribute less to the background human EEG (Gotman, 2008; Lam et al., 2017). The recordings analysed herein are perhaps more analogous to ECoG or depth electrode recordings in humans. In this scenario, the approach of modelling activity recorded from invasive electrodes has shown promise in predicting the outcome of surgery in people with diverse “focal” epilepsies (Goodfellow et al., 2017; Lopes et al., 2017; Sinha et al., 2017; Lopes et al., 2018). Our study advances our understanding of such approaches and demonstrates a framework that allows for their experimental validation.

References

Aarts JHP, Binnie CD, Smit AM, Wilkins AJ (1984) Selective Cognitive Impairment during Focal and Generalized Epileptiform EEG Activity. Brain 107:293-308.

Arabadzisz D, Antal K, Parpan F, Emri Z, Fritschy J-M (2005) Epileptogenesis and chronic seizures in a mouse model of temporal lobe epilepsy are associated with distinct EEG patterns and selective neurochemical alterations in the contralateral hippocampus. Experimental Neurology 194:76-90.

Bartolomei F, Lagarde S, Wendling F, McGonigal A, Jirsa V, Guye M, Bénar C (2017) Defining epileptogenic networks: Contribution of SEEG and signal analysis. Epilepsia:1-17.

584 Benjamini Y, Hochberg Y (1995) Controlling the False Discovery Rate: A Practical and
585 Powerful Approach to Multiple Testing. Journal of the Royal Statistical Society Series B
586 (Methodological) 57:289-300.
587 Borg I, Groenen PJF (2005) Modern multidimensional scaling: Theory and applications. New
588 York, NY: Springer Science & Business Media.
589 Bouilleret V, Ridoux V, Depaulis A, Marescaux C, Nehlig A, Le Gal La Salle G (1999)
590 Recurrent seizures and hippocampal sclerosis following intrahippocampal kainate
591 injection in adult mice: electroencephalography, histopathology and synaptic
592 reorganization similar to mesial temporal lobe epilepsy. Neuroscience 89:717-729.
593 Chauvière L, Doublet T, Ghestem A, Siyoucef SS, Wendling F, Huys R, Jirsa V, Bartolomei F,
594 Bernard C (2012) Changes in interictal spike features precede the onset of temporal lobe
595 epilepsy. Annals of Neurology 71:805-814.
596 Chowdhury FA, Woldman W, FitzGerald THB, Elwes RDC, Nashef L, Terry JR, Richardson
597 MP (2014) Revealing a Brain Network Endophenotype in Families with Idiopathic
598 Generalised Epilepsy. PLOS ONE 9:e110136.
599 Christodoulakis M, Hadjipapas A, Papathanasiou ES, Anastasiadou M, Papacostas SS, Mitsis
600 GD (2015) On the Effect of Volume Conduction on Graph Theoretic Measures of Brain
601 Networks in Epilepsy. In: Modern Electroencephalographic Assessment Techniques:
602 Theory and Applications (Sakkalis V, ed), pp 103-130. New York, NY: Springer New
603 York.
604 Coito A, Plomp G, Genetti M, Abela E, Wiest R, Seeck M, Michel CM, Vulliemoz S (2015)
605 Dynamic directed interictal connectivity in left and right temporal lobe epilepsy.
606 Epilepsia 56:207-217.
607 Dichter MA (2009) Emerging concepts in the pathogenesis of epilepsy and epileptogenesis.
608 Archives of Neurology 66:443-447.
609 Englot DJ, Hinkley LB, Kort NS, Imber BS, Mizuiri D, Honma SM, Findlay AM, Garrett C,
610 Cheung PL, Mantle M, Tarapore PE, Knowlton RC, Chang EF, Kirsch HE, Nagarajan SS
611 (2015) Global and regional functional connectivity maps of neural oscillations in focal
612 epilepsy. Brain 138:2249-2262.
613 Ermentrout G, Kopell N (1986) Parabolic Bursting in an Excitable System Coupled with a Slow
614 Oscillation. SIAM Journal on Applied Mathematics 46:233-253.
615 Gill RS, Mirsattari SM, Leung LS (2017) Resting state functional network disruptions in a kainic
616 acid model of temporal lobe epilepsy. NeuroImage: Clinical 13:70-81.
617 Goldberg EM, Coulter DA (2013) Mechanisms of epileptogenesis: a convergence on neural
618 circuit dysfunction. Nat Rev Neurosci 14:337-349.
619 Golub GH, Loan CFV (1996) Matrix computations (3rd ed.): Johns Hopkins University Press.
620 Goodfellow M, Rummel C, Abela E, Richardson MP, Schindler K, Terry JR (2016) Estimation
621 of brain network ictogenicity predicts outcome from epilepsy surgery. Scientifc Reports
622 6:29215.
623 Goodfellow M, Rummel C, Abela E, Richardson MP, Schindler K, Terry JR (2017) Computer
624 models to inform epilepsy surgery strategies: prediction of postoperative outcome. Brain
625 140:e30-e30.
626 Gotman J (2008) Epileptic networks studied with EEG-fMRI. Epilepsia 49:42-51.
627 Gröticke I, Hoffmann K, Löscher W (2008) Behavioral alterations in a mouse model of temporal
628 lobe epilepsy induced by intrahippocampal injection of kainate. Experimental Neurology
629 213:71-83.
630 Häussler U, Bielefeld L, Froriep UP, Wolfart J, Haas CA (2012) Septotemporal Position in the
631 Hippocampal Formation Determines Epileptic and Neurogenic Activity in Temporal
632 Lobe Epilepsy. Cerebral Cortex 22:26-36.

633 Hebbink J, Meijer H, Huiskamp G, van Gils S, Leijten F (2017) Phenomenological network
634 models: Lessons for epilepsy surgery. Epilepsia 58:e147-e151.
635 Hentschke H, Stüttgen MC (2011) Computation of measures of effect size for neuroscience data
636 sets. 34:1887-1894.
637 Huneau C, Benquet P, Dieuset G, Biraben A, Martin B, Wendling F (2013) Shape features of
638 epileptic spikes are a marker of epileptogenesis in mice. Epilepsia 54:2219-2227.
639 Khambhati AN, Davis KA, Lucas TH, Litt B, Bassett DS (2016) Virtual cortical resection
640 reveals push-pull network control preceding seizure evolution. Neuron 91:1170-1182.
641 Lam AD, Deck G, Goldman A, Eskandar EN, Noebels J, Cole AJ (2017) Silent hippocampal
642 seizures and spikes identified by foramen ovale electrodes in Alzheimer's disease. Nat
643 Med 23:678-680.
644 Lévesque M, Avoli M (2013) The kainic acid model of temporal lobe epilepsy. Neuroscience &
645 Biobehavioral Reviews 37:2887-2899.
646 Li Y, Zhang Z-L (2012) Digraph Laplacian and the Degree of Asymmetry. Internet Mathematics
647 8:381-401.
648 Lopes Da Silva FH, Gorter JA, Wadman WJ (2012) Epilepsy as a dynamic disease of neuronal
649 networks. Handbook of Clinical Neurology 107:35-62.
650 Lopes MA, Richardson MP, Abela E, Rummel C, Schindler K, Goodfellow M, Terry JR (2017)
651 An optimal strategy for epilepsy surgery: Disruption of the rich-club? PLOS
652 Computational Biology 13:e1005637.
653 Lopes MA, Richardson MP, Abela E, Rummel C, Schindler K, Goodfellow M, Terry JR (2018)
654 Elevated Ictal Brain Network Ictogenicity Enables Prediction of Optimal Seizure Control.
655 Frontiers in Neurology 9:98.
656 Löscher W, Brandt C (2010) Prevention or Modification of Epileptogenesis after Brain Insults:
657 Experimental Approaches and Translational Research. Pharmacological Reviews 62:668.
658 Löscher W, Hirsch LJ, Schmidt D (2015) The enigma of the latent period in the development of
659 symptomatic acquired epilepsy — Traditional view versus new concepts. Epilepsy &
660 Behavior 52:78-92.
661 Lowenstein DH (2009) Epilepsy after head injury: An overview. Epilepsia 50:4-9.
662 Mathon B, Bielle F, Samson S, Plaisant O, Dupont S, Bertrand A, Miles R, Nguyen-Michel V-H,
663 Lambrecq V, Calderon-Garcidueñas AL, Duyckaerts C, Carpentier A, Baulac M, Cornu
664 P, Adam C, Clemenceau S, Navarro V (2017) Predictive factors of long-term outcomes
665 of surgery for mesial temporal lobe epilepsy associated with hippocampal sclerosis.
666 Epilepsia 58:1473-1485.
667 Matlab Release 2018b. Natick, Massachusetts, United States.: The MathWorks, Inc.
668 Melozzi F, Woodman MM, Jirsa VK, Bernard C (2017) The Virtual Mouse Brain: A
669 Computational Neuroinformatics Platform to Study Whole Mouse Brain Dynamics.
670 eneuro.
671 Mohamed A, Wyllie E, Ruggieri P, Kotagal P, Babb T, Hilbig A, Wylie C, Ying Z, Staugaitis S,
672 Najm I, Bulacio J, Foldvary N, Lüders H, Bingaman W (2001) Temporal lobe epilepsy
673 due to hippocampal sclerosis in pediatric candidates for epilepsy surgery. Neurology
674 56:1643-1649.
675 Moseley BD, Sinha S, Meyer FB, Marsh WR, Britton JW (2012) Long term outcomes in patients
676 with preoperative generalized interictal epileptiform abnormalities following
677 amygdalohippocampectomy. Epilepsy Research 99:171-175.
678 Niso G, Carrasco S, Gudín M, Maestú F, del-Pozo F, Pereda E (2015) What graph theory
679 actually tells us about resting state interictal MEG epileptic activity. NeuroImage:
680 Clinical 8:503-515.

Nissen IA, Stam CJ, Reijneveld JC, van Straaten IECW, Hendriks EJ, Baayen JC, De Witt Hamer PC, Idema S, Hillebrand A (2017) Identifying the epileptogenic zone in interictal resting-state MEG source-space networks. Epilepsia 58:137-148.

Otte WM, Dijkhuizen RM, van Meer MPA, van der Hel WS, Verlinde SAMW, van Nieuwenhuizen O, Viergever MA, Stam CJ, Braun KPJ (2012) Characterization of Functional and Structural Integrity in Experimental Focal Epilepsy: Reduced Network Efficiency Coincides with White Matter Changes. PLOS ONE 7:e39078.

Proix T, Bartolomei F, Guye M, Jirsa VK (2017) Individual brain structure and modelling predict seizure propagation. Brain 140:641-654.

Riban V, Bouilleret V, Pham-Lê BT, Fritschy JM, Marescaux C, Depaulis A (2002) Evolution of hippocampal epileptic activity during the development of hippocampal sclerosis in a mouse model of temporal lobe epilepsy. Neuroscience 112:101-111.

Rummel C, Abela E, Andrzejak RG, Hauf M, Pollo C, Müller M, Weisstanner C, Wiest R, Schindler K (2015) Resected Brain Tissue, Seizure Onset Zone and Quantitative EEG Measures: Towards Prediction of Post-Surgical Seizure Control. PLOS ONE 10:e0141023.

Salami P, Lévesque M, Benini R, Behr C, Gotman J, Avoli M (2014) Dynamics of interictal spikes and high-frequency oscillations during epileptogenesis in temporal lobe epilepsy. Neurobiology of Disease 67:97-106.

Schmidt H, Petkov G, Richardson MP, Terry JR (2014) Dynamics on Networks: The Role of Local Dynamics and Global Networks on the Emergence of Hypersynchronous Neural Activity. PLOS Computational Biology 10:e1003947.

Schmidt H, Woldman W, Goodfellow M, Chowdhury FA, Koutroumanidis M, Jewell S, Richardson MP, Terry JR (2016) A computational biomarker of idiopathic generalized epilepsy from resting state EEG. Epilepsia 57:e200-e204.

Schreiber T, Schmitz A (1996) Improved Surrogate Data for Nonlinearity Tests. Physical Review Letters 77:635-638.

Sheybani L, Birot G, Contestabile A, Seeck M, Zoltan Kiss J, Schaller K, Michel CM, Quairiaux C (2018) Electrophysiological evidence for the development of a self-sustained large-scale epileptic network in the kainate mouse-model of temporal lobe epilepsy. Journal of Neuroscience.

Sinha N, Dauwels J, Kaiser M, Cash SS, Brandon Westover M, Wang Y, Taylor PN (2017) Predicting neurosurgical outcomes in focal epilepsy patients using computational modelling. Brain 140:319-332.

Smith EH, Schevon CA (2016) Toward a Mechanistic Understanding of Epileptic Networks. Current Neurology and Neuroscience Reports 16:97.

Soriano MC, Niso G, Clements J, Ortín S, Carrasco S, Gudín M, Mirasso CR, Pereda E (2017) Automated Detection of Epileptic Biomarkers in Resting-State Interictal MEG Data. Frontiers in Neuroinformatics 11:43.

Tracy JI, Doucet GE (2015) Resting-state functional connectivity in epilepsy: growing relevance for clinical decision making. Current Opinion in Neurology 28.

van Dellen E, Douw L, Hillebrand A, de Witt Hamer PC, Baayen JC, Heimans JJ, Reijneveld JC, Stam CJ (2014) Epilepsy surgery outcome and functional network alterations in longitudinal MEG: A minimum spanning tree analysis. NeuroImage 86:354-363.

Wang HE, Bénar CG, Quilichini PP, Friston KJ, Jirsa VK, Bernard C (2014) A systematic framework for functional connectivity measures. 8.

Woldman W, Terry JR (2015) Multilevel Computational Modelling in Epilepsy: Classical Studies and Recent Advances. In: Validating Neuro-Computational Models of Neurological and Psychiatric Disorders (Bhattacharya BS, Chowdhury FN, eds), pp 161-188. Cham: Springer International Publishing.

731 World Health Organization (2019) Epilepsy. In: Epilepsy. https://www.who.int/news-room/fact-
732 sheets/detail/epilepsy.
733
734

Legends

Figure 1. Criteria for excluding recordings from analysis. Number of segments selected in a recording vs number of non-zero elements in the average adjacency matrix estimated from all the segments in the recording. Each dot represents a single recording. Recordings represented by the encircled dots were excluded from the analysis. **A**, matrices estimated using C^{ABS}; **B**, matrices estimated using C^{MAX}; **C**, matrices estimated using C^{MIN}. All the method produced average adjacency matrices with similar number of non-zero elements.

Figure 2. Analysis of background functional connectivity reveals changes over the time course of epileptogenesis. A, **E** and **I** Individual connectivity matrices represented as dots in the first two principal dimensions of the multidimensional scaling of Frobenius distances between the individual connectivity matrices. Each dot represents a single matrix (green – day 0; yellow – day 7; red – day 28; grey – Sham control; empty symbols: circle, diamond and square represent the median of the connectivity matrices). The first three principal MDS dimensions represent around 70% of the relations encoded in the raw Frobenius distances (R^2_{ABS}=0.66, R^2_{MAX}=0.72, R^2_{MIN}=0.7, R is Pearson's correlation coefficient between the Frobenius distances in the matrix space and the Euclidian distances in the reconstructed space); for clarity only the first two coordinates are plotted. **B-D**, **F-H**, **J-L**, Median functional connectivity matrices (indicated with empty symbols in panels **A**, **E** and **I**) resulting from the three different measures at different days with color-coded connection weights (Day 0 over 11 matrices, Day 7 over 6 matrices, Day 28 over 8 matrices; different numbers of matrices for individual days due to quality of recordings, see Materials and Methods for details).

Figure 3. Illustration of changes of network properties over the time-course of epileptogenesis. A-C, **E-G**, **I-K**, Median degree imbalance at individual nodes; blue indicates indegree>outdegree, red indicates indegree<outdegree. Value of the degree imbalance is colour and size coded, larger and darker dots indicate higher degree imbalance. Dots filled in black have a median that is significantly different than the median on day 0 (FDR<0.1, two-sided Wilcoxon-Mann-Whitney test with Benjamini-Hochberg correction for 30 nodes, effect size AUROC<0.2 for blue nodes or >0.8 for red nodes; exact p-values and effect sizes are presented in Extended data Figure 3-1). Grey arrows show topology of functional connectivity networks on different days illustrated using the strongest 5% of connections of the median connectivity matrices shown in Figure 2. **D**, **H** and **L**, boxplots showing the degree imbalance of the individual connectivity matrices.

Figure 4. Illustration of changes in spatial distribution of node ictogenicity. A-C, **D-F**, **G-I** Mean values of NI. Grey arrows are the strongest 5% of connections of the median networks. Value of the NI is colour and size coded, larger and darker dots indicate higher NI. Dots filled in black have significantly higher median NI than the median on day 0 (FDR<0.1 one-sided Wilcoxon-Mann-Whitney test with Benjamini-Hochberg FDR correction for 30 nodes, effect size AUROC>0.8; exact p-values and effect sizes are presented in Extended data Figure 4-1). Shaded region in panel **H** and **I** shows nodes affected by the TTX silencing; identified from Fig. 22B (Sheybani et al., 2018).

Table 1. Statistical table matrix. Columns are: part of the results section, the structure of the data, statistical test, description of the significance levels.

Table 2. Statistical analysis of network properties for the three kinds of connectivity matrices. Table contains values of the Benjamini-Hochberg FDR for the Kruskal-Wallis test for

785 comparison of medians of measures on Day 0, Day 7 and Day 28. In brackets post-hoc effect
786 sizes quantified with AUROC: (Day 0 vs Day 7; Day 0 vs Day 28). In bold values with FDR<0.1
787 and AUROC<0.2 or AUROC>0.8.

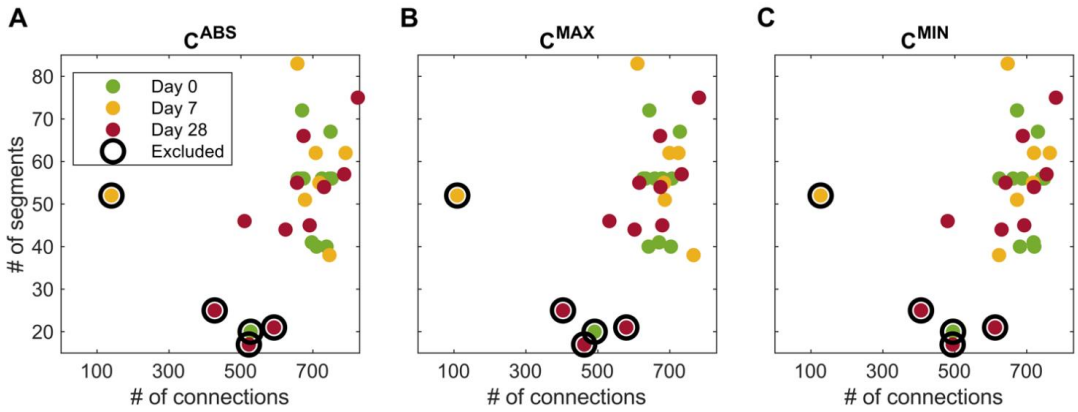

Figure 1. Criteria for excluding recordings from analysis. Number of segments selected in a recording vs number of non-zero elements in the average adjacency matrix estimated from all the segments in the recording. Each dot represents a single recording. Recordings represented by the encircled dots were excluded from the analysis. **A**, matrices estimated using C^{ABS}; **B**, matrices estimated using C^{MAX}; **C**, matrices estimated using C^{MIN}. All the method produced average adjacency matrices with similar number of non-zero elements.

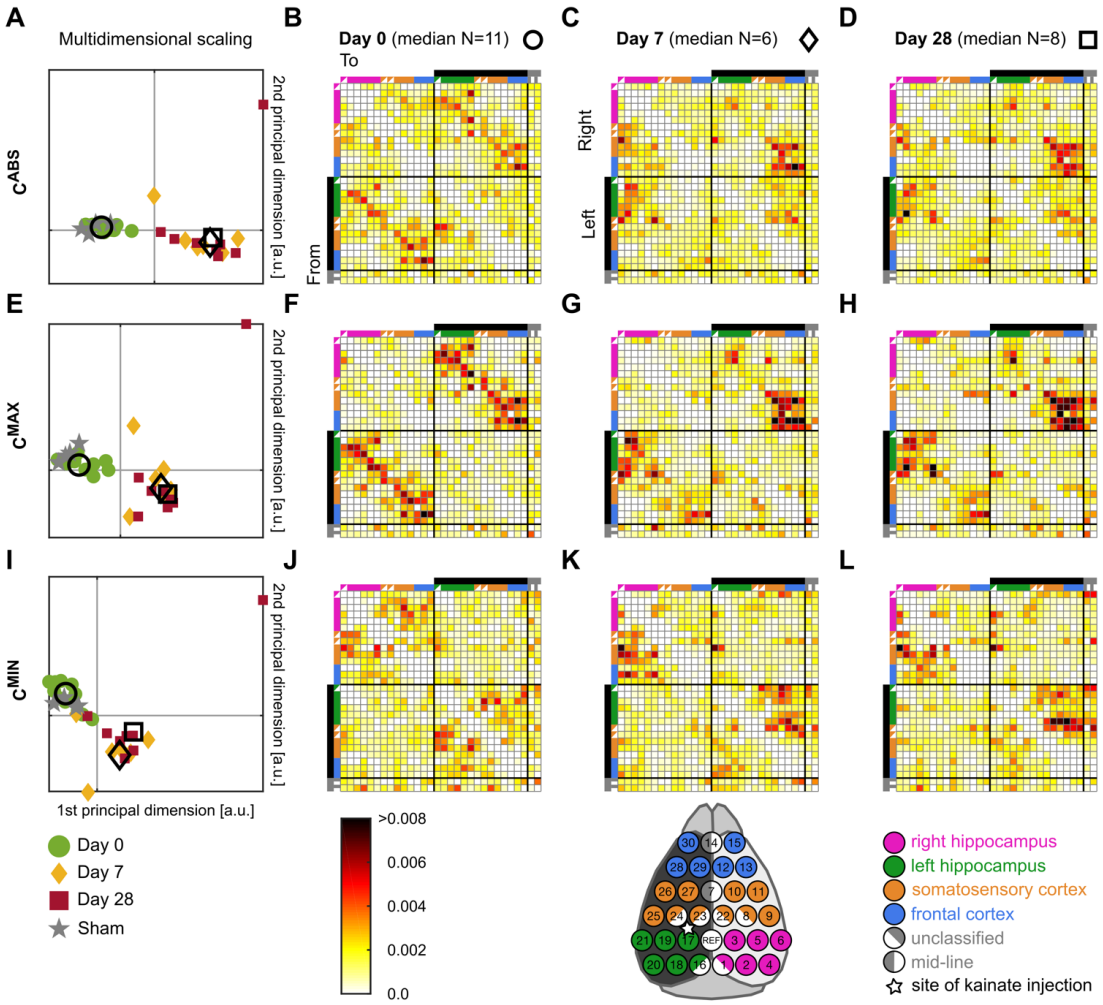

Figure 2. Analysis of background functional connectivity reveals changes over the time course of epileptogenesis. A, **E** and **I** Individual connectivity matrices represented as dots in the first two principal dimensions of the multidimensional scaling of Frobenius distances between the individual connectivity matrices. Each dot represents a single matrix (green – day 0; yellow – day 7; red – day 28; grey – Sham control; empty symbols: circle, diamond and square represent the median of the connectivity matrices). The first three principal MDS dimensions represent around 70% of the relations encoded in the raw Frobenius distances (R^2_{ABS}=0.66, R^2_{MAX}=0.72, R^2_{MIN}=0.7, R is Pearson's correlation coefficient between the Frobenius distances in the matrix space and the Euclidian distances in the reconstructed space); for clarity only the first two coordinates are plotted. **B-D**, **F-H**, **J-L**, Median functional connectivity matrices (indicated with empty symbols in panels **A**, **E** and **I**) resulting from the three different measures at different days with color-coded connection weights (Day 0 over 11 matrices, Day 7 over 6 matrices, Day 28 over 8 matrices; different numbers of matrices for individual days due to quality of recordings, see Materials and Methods for details).

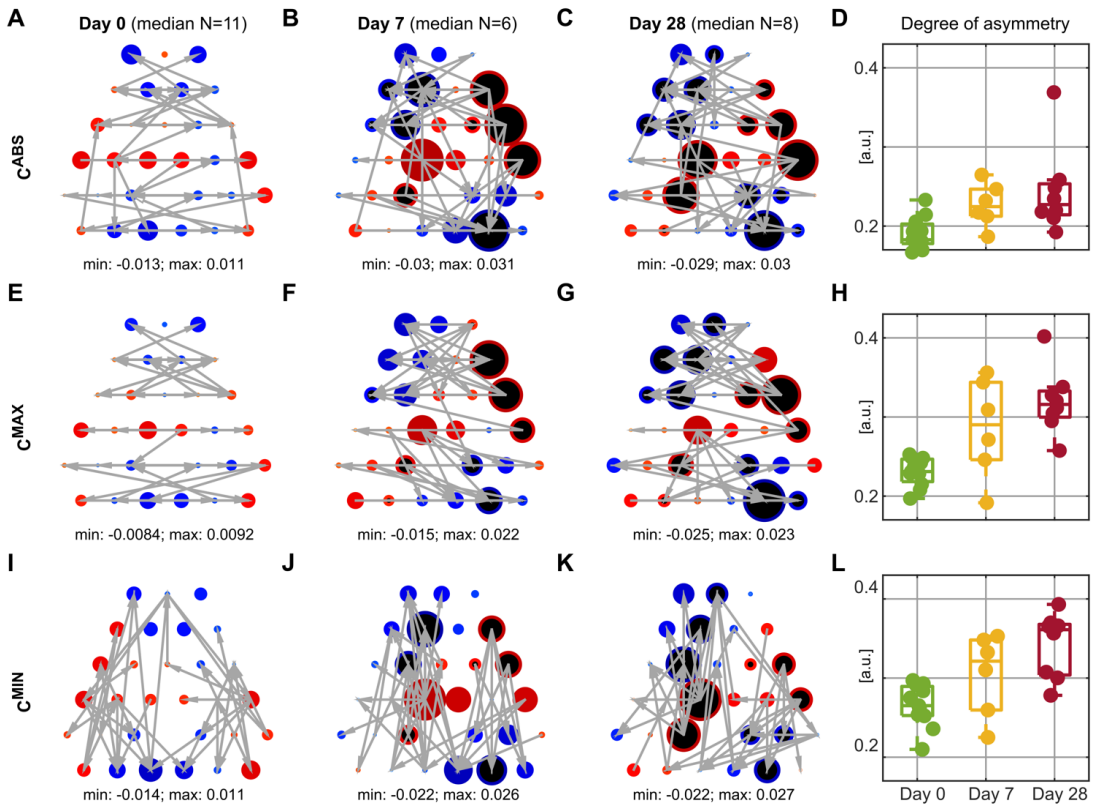

Figure 3. Illustration of changes of network properties over the time-course of epileptogenesis. A-C, **E-G**, **I-K**, Median degree imbalance at individual nodes; blue indicates indegree>outdegree, red indicates indegree<outdegree. Value of the degree imbalance is colour and size coded, larger and darker dots indicate higher degree imbalance. Dots filled in black have a median that is significantly different than the median on day 0 (FDR<0.1, two-sided Wilcoxon-Mann-Whitney test with Benjamini-Hochberg correction for 30 nodes, effect size AUROC<0.2 for blue nodes or >0.8 for red nodes; exact p-values and effect sizes are presented in Extended data Figure 3-1). Grey arrows show topology of functional connectivity networks on different days illustrated using the strongest 5% of connections of the median connectivity matrices shown in Figure 2. **D**, **H** and **L**, boxplots showing the degree imbalance of the individual connectivity matrices.

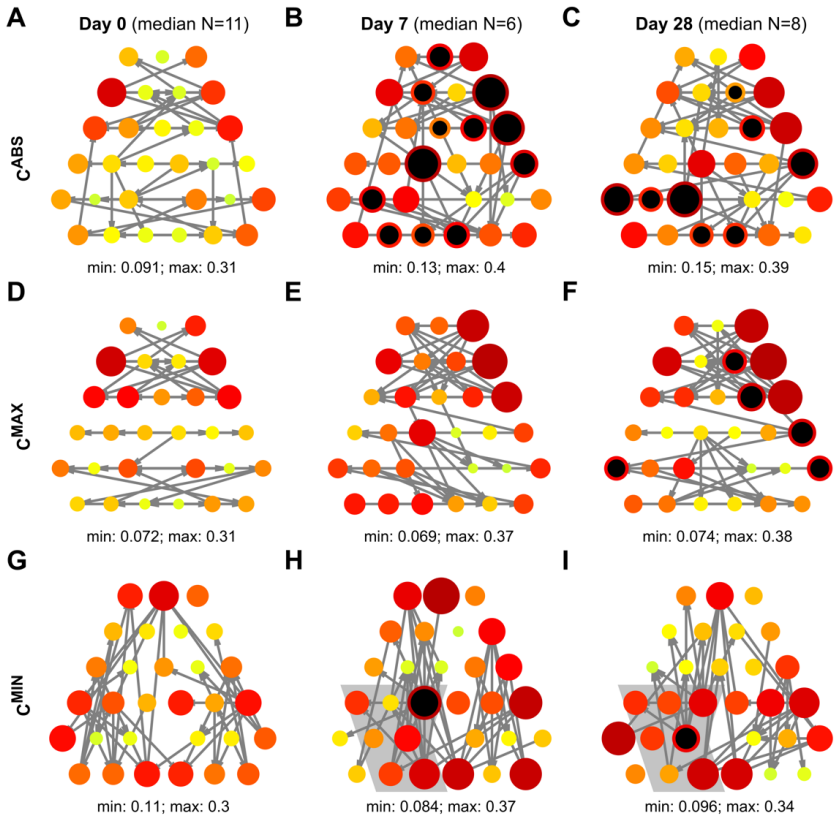

Figure 4. Illustration of changes in spatial distribution of node ictogenicity. A-C, D-F, G-I Mean values of NI. Grey arrows are the strongest 5% of connections of the median networks. Value of the NI is colour and size coded, larger and darker dots indicate higher NI. Dots filled in black have significantly higher median NI than the median on day 0 (FDR<0.1 one-sided Wilcoxon-Mann-Whitney test with Benjamini-Hochberg FDR correction for 30 nodes, effect size AUROC>0.8; exact p-values and effect sizes are presented in Extended data Figure 4-1). Shaded region in panel **H** and **I** shows nodes affected by the TTX silencing; identified from Fig. 22B (Sheybani et al., 2018).

838 **Table 1. Statistical table matrix.** Columns are: part of the results section, the structure of the
839 data, statistical test, description of the significance levels.
840

RESULTS	DATA STRUCTURE	STATISTICAL TEST	POWER OR CONFIDENCE INTERVALS
Figure 3. A-C, E-G, I-K	No assumptions about the distributions of the degree imbalance on each of the three days.	Two-sided Wilcoxon-Mann-Whitney test with Benjamini-Hochberg multiple comparison/ false discovery ratio (FDR) correction for 30 nodes. Separate comparison for: Day 0 vs. Day 7 and Day 0 and Day 28. We use two-sided test because we expect to see increase and decrease of degree imbalance.	Panel B: FDR ≤ 0.08, AUROC<0.2 or AUROC>0.8; Panel C: FDR ≤ 0.08, AUROC<0.2 or AUROC>0.8; Panel D: FDR ≤ 0.1, AUROC<0.2 or AUROC>0.8; Panel E: FDR ≤ 0.07, AUROC<0.2 or AUROC>0.8; Panel G: FDR ≤ 0.07, AUROC<0.2 or AUROC>0.9; Panel H: FDR ≤ 0.07, AUROC<0.2. or AUROC>0.9; See Extended data Figure 3-1 for values.
Figure 3. D, H and L and Table 2.	No assumptions about the distributions of the network measures.	The Kruskal-Wallis test (non-parametric ANOVA) with Benjamini-Hochberg multiple comparison/ false discovery ratio (FDR) correction for 20 analysed measures.	FDR and AUROC values are reported in the Table 2
Figure 4.	No assumptions about the distributions of the node ictogenicity on each of the three days.	One-sided Wilcoxon-Mann-Whitney test with Benjamini-Hochberg multiple comparison/ false discovery ratio (FDR) correction for 30 nodes. Separate comparison for: Day 0 vs. Day 7 and Day 0 and Day 28. We use one-sided test because only test increase of node icotgenicity.	Panel B: FDR ≤ 0.1, AUROC>0.8; Panel C: FDR ≤ 0.09, AUROC>0.8; Panel E: FDR ≤ 0.08, AUROC>0.8; Panel G: FDR ≤ 0.02, AUROC=1; Panel H: FDR ≤ 0.01, AUROC<0.9. See Extended data Figure 4-1 for values.

841

Table 2. Statistical analysis of network properties for the three kinds of connectivity matrices. Table contains values of the Benjamini-Hochberg FDR for the Kruskal-Wallis test for comparison of medians of measures on Day 0, Day 7 and Day 28. In brackets post-hoc effect sizes quantified with AUROC: (Day 0 vs Day 7; Day 0 vs Day 28). In bold values with FDR<0.1 and AUROC<0.2 or AUROC>0.8.

NAME OF THE NETWORK PROPERTY	C^{ABS}	C^{MAX}	C^{MIN}
Mean weighted outdegree	0.69	0.83	0.5
Variance of weighted outdegree	**0.055** (0.23; **0.13)**	**0.035** **(0.17; 0.13)**	0.12
Spectral norm	**0.0099** **(0; 0.091)**	**0.0083** **(0.061; 0.046)**	**0.026** **(0.11; 0.13)**
Frobenius norm	0.42	0.47	0.27
Mean neighbour weighted outdegree	0.21	0.24	0.4
Variance of neighbour weighted outdegree	**0.0099** **(0.03; 0.079)**	**0.0131** **(0.076; 0.1)**	**0.0233** (0.71; **0.89)**
Mean betweenness	0.20	0.75	0.66
Variance of betweenness	**0.098** **(0.12;** 0.48**)**	0.44	0.3
Mean pagerank	0.4	0.96	0.58
Variance of pagerank	0.17	0.47	0.27
Mean length of the shortest path between two nodes	0.29	0.47	0.4
Variance of length of the shortest paths	0.17	0.8	0.4
Mean harmonic closeness centrality	0.29	0.47	0.4
Variance of harmonic closeness centrality	**0.068** **(0.91;** 0.62**)**	0.2	0.5
Assortative mixing (Pearson's total weighted degree correlation)	0.17	0.66	0.058
S-metric - sum of the product of nodal degrees across edges	0.81	0.5	0.78
Degree of asymmetry – largest eigenvalue of the skew-symmetric part of the Laplacian of a directed graph (Li and Zhang, 2012).	**0.026** **(0.14; 0.1)**	**0.011** (0.21; **0)**	**0.026** (0.26; **0.045)**
Mean spectrum – mean of eigenvalues of symmetric part of the Laplacian matrix of the directed graph (Li and Zhang, 2012).	0.74	0.8	0.14
Variance of spectrum – variance of eigenvalues of symmetric part of the Laplacian matrix of the directed graph (Li and Zhang, 2012).	0.4	0.25	0.88
Maximum of spectrum – largest eigenvalue of symmetric part of the Laplacian matrix of the directed graph (Li and Zhang, 2012).	0.17	0.25	0.76

Extended data

Figure 3-1. Detailed illustration of changes in spatial distribution of degree imbalance (DI). **A-C** Boxplots of distributions of DI values on each node on Day 0 (green), Day 7 (yellow) and Day 28 (Red). Shaded yellow bar indicates significant difference between Day 0 and Day 7. Shaded red bar indicates significant difference between Day 0 and Day 28. Text labels are: first row FDR, second row (AUROC) for comparison of Day 0 and Day 28; third row FDR and fourth row (AUROC) for comparison of Day 0 and Day 7. Two-sided Wilcoxon-Mann-Whitney test with Benjamini-Hochberg FDR correction for 30 nodes, effect size measured as AUROC.

Figure 4-1. Detailed illustration of changes in spatial distribution of node ictogenicity (NI). **A-C** Boxplots of distributions of NI values on each node on Day 0 (green), Day 7 (yellow) and Day 28 (Red). Shaded yellow bar indicates significant difference between Day 0 and Day 7. Shaded red bar indicates significant difference between Day 0 and Day 28. Text labels are: first row FDR, second row (AUROC) for comparison of Day 0 and Day 28; third row FDR and fourth row (AUROC) for comparison of Day 0 and Day 7. One-sided Wilcoxon-Mann-Whitney test with Benjamini-Hochberg FDR correction for 30 nodes, effect size measured as AUROC.